K. Jin
Department of Mechanical Science
and Engineering,
University of Illinois at Urbana-Champaign,
Urbana, IL 61820
e-mail: kaijin2@illinois.edu

S. P. Vanka[1]
Department of Mechanical Science
and Engineering,
University of Illinois at Urbana-Champaign,
Urbana, IL 61820
e-mail: spvanka@illinois.edu

B. G. Thomas
Department of Mechanical Science
and Engineering,
University of Illinois at Urbana-Champaign,
Urbana, IL 61820
e-mail: bgthomas@illinois.edu

Three-Dimensional Flow in a Driven Cavity Subjected to an External Magnetic Field

In this paper, we study the three-dimensional (3D) flow of an electrically conducting fluid in a cubic cavity with the top wall moving and subjected to an external magnetic field. The governing flow and electromagnetic field equations are integrated by a second-order space and time accurate numerical scheme, implemented on a graphics processing unit (GPU) with high parallel efficiency. Solutions for several Reynolds and Stuart numbers have been obtained on sufficiently fine grids to achieve grid independent solutions. As expected, the magnetic field significantly influences the circulation in the cavity and modifies the shape and locations of the primary and secondary eddies. The observed flow patterns are illustrated graphically as well as through selected line plots and tabulated data. With increasing magnetic field strength, the center of the primary eddy is seen to shift to the top right corner. Further, situations where the flow is unsteady in the absence of the magnetic field have become steady after a certain value of the magnetic interaction parameter. [DOI: 10.1115/1.4029731]

1 Introduction

The flow in a cavity driven by the shear induced by motion of one of the walls has been a classical problem in fluid mechanics and numerous research papers have appeared on the characterization of the vortices generated in such a flow [1–41]. The widely studied case is the flow generated by the motion of the top wall of a square cavity in which a primary recirculating eddy and two smaller corner eddies at the bottom left and bottom right corners are generated. Bench-mark solutions of two-dimensional (2D) Newtonian flow in a square cavity have been published by several researchers, e.g., Refs. [1–10]. A number of studies for 3D flow in a cube driven by the top wall have also been published, e.g., Refs. [17–41], illustrating the rich 3D flow structures that are generated due to the presence of the walls in the spanwise direction and by the instabilities of the curved streamlines. It is seen that on the bottom wall, streamwise vortical structures akin to Taylor–Göertler-like (TGL) vortices are generated after a critical Reynolds number is exceeded. In addition, the flow becomes progressively more complex, eventually becoming unsteady and turbulent [36–38]. The rectangular shapes have been the most widely studied geometries and have become standard problems for development and validation of computational algorithms and codes. A smaller number of studies have been performed on cavities of other shapes, such as trapezoidal [42–44], triangular [42,45,46], semi-circular [47,48], and other complex shapes [49].

When a magnetic field is applied to an electrically conducting moving fluid, an electric current field is generated. This current field, together with the magnetic field, generates a force field ($\mathbf{F} = \mathbf{J} \times \mathbf{B}$, where $\mathbf{J}$ and $\mathbf{B}$ are electrical current and magnetic field vectors, respectively) that brakes the fluid motion. The modified velocity field in turn changes the current field and the electromagnetic force on fluid. This two-way interaction has profound effects on transport phenomena in various industries such as steel making, crystal growth, welding, aluminum smelting, fusion power generation, and magnetohydrodynamics (MHD) coal fired power plants. Such MHD forces have also been known to modify the turbulence structure including completely laminarizing a turbulent flow at sufficiently large magnetic fields and interaction parameters.

The effect of a magnetic field on a driven cavity flow is quite interesting because of the complex vortical structures that interact in a complex way with the magnetic field. To our knowledge, only a limited number of studies have examined such flows, primarily in two dimensions. Al-Salem et al. [50] used a finite volume method to investigate the effect of a magnetic field on heat transfer in a lid-driven cavity with bottom wall subject to a linear temperature distribution. They found that increasing the Hartmann number decreases the strength of the flow and therefore the heat transfer rate is also reduced. Their study also showed that due to the nonuniform temperature distribution along the bottom wall, the heat transfer rate can be improved if the lid moves in the same direction as the wall temperature decreases. Oztop et al. [51] studied the effect of a magnetic field on heat transfer in a two-dimensional lid-driven square cavity with a corner heater for several different Hartmann numbers and Grashof numbers at a fixed Reynolds number of $\mathrm{Re} = 100$. The lid was moved in the positive coordinate direction, while the magnetic field was applied in the negative coordinate direction. They found that an increase in Hartmann number causes the top eddy to shrink and become closer to the moving lid, and simultaneously the bottom eddy becomes larger. The strength of the fluid circulation was reduced and the thickness of the thermal boundary layer was increased as the Hartmann number was increased. The local Nusselt number along the bottom wall consequently decreased with Hartmann number.

Sivasankaran et al. [52] also used a finite volume code to investigate the mixed convection in a square lid driven cavity with sinusoidal boundary temperature at the vertical walls in the presence of an external magnetic field for a fixed Reynolds number of 100. Results for three different Hartmann numbers (zero, 25, and 100) are reported and they found that increasing the Hartmann number restricts the flow circulation in the region close to the top lid. Their results also showed that if forced convection dominates the flow behavior, increasing the Hartmann number does not affect the heat transfer at the side walls. However, if the flow is in the regime of buoyancy-driven convection, increasing the Hartmann number leads to decrease of total heat transfer rate. Yu et al. [53] studied the effect of Hartmann number on natural convection heat transfer in a 2D square cavity at different Rayleigh numbers

[1]Corresponding author.

Contributed by the Fluids Engineering Division of ASME for publication in the Journal of Fluids Engineering. Manuscript received November 16, 2014; final manuscript received January 20, 2015; published online March 26, 2015. Assoc. Editor: Shizhi Qian.

 Copyright © 2015 by ASME

Downloaded From: http://asmedigitalcollection.asme.org/ on 03/26/2015 Terms of Use: http://asme.org/terms

using a streamfunction–vorticity scheme. In their study, the vertical walls of the cavity were maintained at different temperatures. For $Ha = 100$ and $Ra = 10^4$, they investigated the effect of inclination angle of the magnetic field. Their results showed that for large Hartmann numbers, the flow structure is highly influenced by the inclination angle of the magnetic field, but the temperature field is not sensitive to the inclination angle if the magnetic field is dominant. In all the above studies [50–53], the Maxwell's equations for the electrical potential were not solved and the effect of Lorentz force on the momentum equations was included by adding a source term which is linearly proportional to the local velocity and square of the external magnetic field (i.e., $F = vB^2\sigma/\rho$).

Shatrov et al. [54] reported results of a 2D square lid-driven cavity flow and linear stability analysis (LSA) of a 3D lid-driven cavity flow problem with external magnetic field applied in the same direction as the moving lid. For the 2D MHD problem, they found that the strength of the eddy is weakened by the external magnetic field. With increasing magnetic field, the primary eddy changes from a circular shape to an elliptical shape. With further increase in the strength of the magnetic field, the secondary eddy begins to occupy the bottom part (from left to right) of the square cavity. Their LSA showed that for the 3D lid-driven cavity the instability of the flow can be dampened by increasing the strength of external magnetic field. For $Re = 3100$, there exist several branches of the neutral stability curve and an increase of the magnetic field strength may lead to a transition from a stable flow to an oscillatory flow.

The 3D flow of a Newtonian fluid in a cube driven by the top wall without a magnetic field has also been the subject a large number of numerical studies. Interest in such studies dates back to 1975 [17] and has been maintained steadily for the past 40 years (e.g., Refs. [17–40]). There have been a variety of techniques used to compute essentially the same flow, albeit with different accuracy, grid, and Reynolds numbers. Finite volume methods [18,19,21,26], finite-element methods [28,30], spectral methods [20,29,32], velocity vorticity methods [22], and Lattice Boltzmann methods [33,36,37] have been used. The primary features observed are nearly the same in all these studies. At low Reynolds numbers, the flow is similar to the flow in a 2D cavity, except for the boundary layers on the spanwise walls (if the spanwise direction is periodic, exactly 2D solutions are obtained). The central plane of the 3D domain consists of a primary eddy and two secondary eddies in the right and left bottom corners. However, the primary feature of 3D analyses is capturing possible 3D structures even in a nominally 2D (i.e. periodic) geometry. For example, at reasonably high Reynolds numbers, it has been observed that the recirculating primary eddy generates centrifugal instabilities [29], and Taylor–Göertler type vortices are formed near the bottom walls [30]. Freitas et al. [18] have applied a finite volume code REBUFFS to study the lid-driven 3D cavity flow at $Re = 3200$ and compared their results with their own experiments. They used a $32 \times 32 \times 45$ grid and the SIMPLE [55] algorithm with QUICK [56] scheme and solved only half of the cavity assuming the flow to be symmetric about the middle plane. They were able to capture that the TGL vortices were also found in the experiments. The size and the location of those vortices were observed to be time dependent. Mean velocities on the central lines of the symmetry plane were satisfactorily compared with laser Doppler velocity measurements at $Re = 3300$.

Based on the above literature study, we conclude that to the best of our knowledge, there have been no published studies which have systematically presented the effect of a magnetic field on an electrical conducting fluid in a 3D lid driven cavity at different Reynolds numbers and for several magnetic field strengths. In the presented work, we have conducted several highly resolved simulations of such flows. Three-dimensional MHD flows are obviously more computationally expensive over 2D simulations. However, with the development of parallel computers, it is now possible to perform large scale 3D flow calculations in reasonable computing times. The GPU is a highly parallel computing platform available on a desktop. The GPU is a highly parallel, multithreaded, many core processor with a large computational power and high memory bandwidth. In recent years, it has been increasingly recognized that the data parallel features of a GPU can be effectively exploited to perform large scale scientific computations to achieve greater speeds without adding to the cost of performing the computation on a CPU. Recently, a considerable amount of interest has been generated on the use of the GPU as a data parallel computing platform [57,58]. A recent review of implementation of computational fluid dynamics (CFD) codes on GPUs has been given in Ref. [57], which refers to a large numbers of papers. Several researchers have developed/ported CFD software to GPUs and found significant speedups (10–50 times depending on algorithm, approach and implementation) over a single core CPU. The GPU is a highly parallel, multithreaded, many core processor with a large computational power and high memory bandwidth.

In this paper, we study the motion of an electrically conducting fluid in a cavity with a moving wall and an external magnetic field. The 3D Navier–Stokes equations are solved using the Harlow–Welch [57] algorithm. A considerable speed-up is obtained by implementing the algorithm on the GPU. Streamline patterns and velocity profiles at the centerlines for different Reynolds numbers and magnetic field strengths are presented. This paper is organized by first describing the governing equations and solution procedure in Sec. 2. The validation and grid independency studies are presented in Sec. 3. Section 4 discusses results of a number of well-resolved calculations. Finally, the important results are summarized.

2 Governing Equations and Solution Procedure

The problem being solved is the flow of an incompressible electrically conducting fluid in an electrically insulated three-dimensional cavity with the top wall moving. The magnetic field is applied in the same direction as the moving wall. In this work, the ratio of the induced magnetic field to the external magnetic field is assumed to be much less than one, and therefore the induced magnetic field generated by electromagnetic induction is neglected. The set of governing equations for this flow is given by Eqs. (1)–(6). The electrical current density $\mathbf{J}$ can be computed through the Ohm's law as given by Eq. (1), and for a well conducting material the current conservation law can be written as Eq. (2). Therefore, the electric potential Φ satisfies Eq. (3). The Lorentz force $\mathbf{F}$ is the cross product of current density and external magnetic field B_0, as given in Eq. (4). The continuity and momentum equations are given by Eqs. (5) and (6), respectively. In the dimensionless equations, distances were nondimensionalized with the height of the cavity L, velocities were nondimensionalized using the moving wall speed U, pressure was nondimensionalized with ρU^2, and time was nondimensionalized with L/U

$$\mathbf{J} = \sigma(-\nabla\Phi + \mathbf{u} \times \mathbf{B}_0) \tag{1}$$

$$\nabla \cdot \mathbf{J} = 0 \tag{2}$$

$$\nabla^2\Phi = \nabla \cdot (\mathbf{u} \times \mathbf{B}_0) \tag{3}$$

$$\mathbf{F} = \mathbf{J} \times \mathbf{B}_0 \tag{4}$$

$$\nabla \cdot \mathbf{u} = 0 \tag{5}$$

$$\frac{\partial \mathbf{u}}{\partial t} + (\mathbf{u} \cdot \nabla)\mathbf{u} = -\nabla p + \frac{1}{\mathrm{Re}}\nabla^2\mathbf{u} + N\mathbf{F} \tag{6}$$

Here, $\mathbf{u} = (u, v, w)$ is the velocity vector; p is the dimensionless pressure; t is dimensionless time; Re is Reynolds number; N is Stuart number (also known as magnetic interaction parameter), which describes the ratio of electromagnetic to inertial forces; and

Downloaded From: http://asmedigitalcollection.asme.org/ on 03/26/2015 Terms of Use: http://asme.org/terms

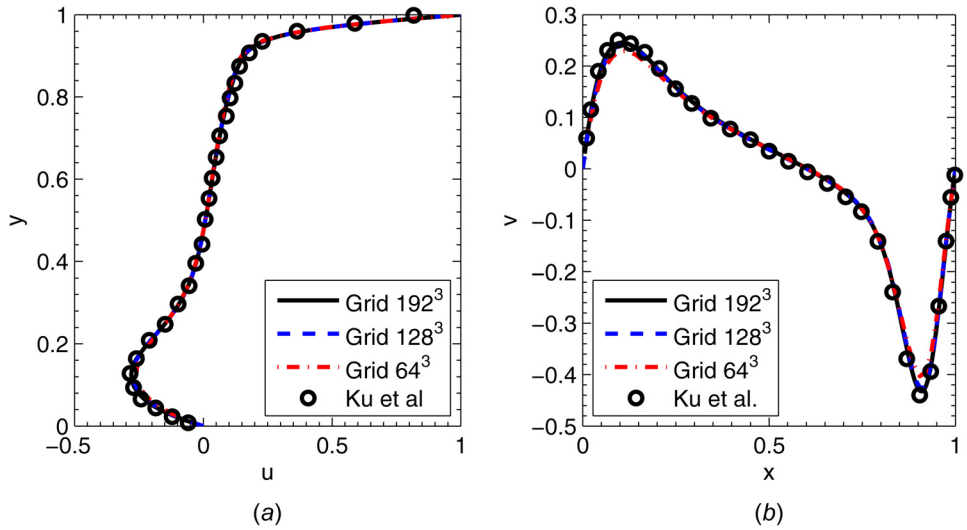

Fig. 1 Comparison of velocity profiles in symmetry plane of a lid-driven cube, Re = 1000

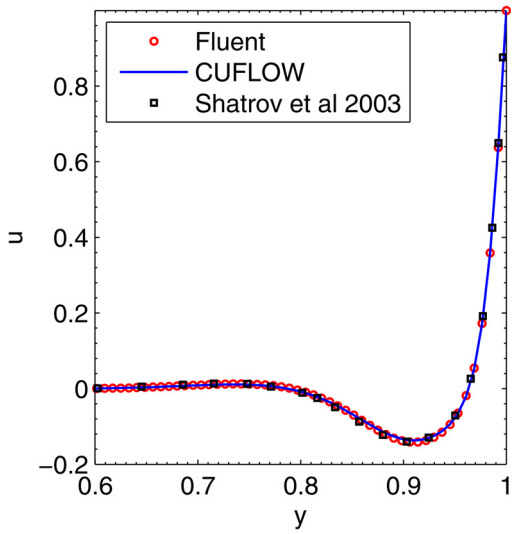

Fig. 2 Validation result of 2D cavity MHD flow at Re = 5000 and *N* = 5

$N = \mathrm{Ha}^2/\mathrm{Re}$, where the Hartmann number Ha is defined as $\mathrm{Ha} = B_0 L(\sigma/\mu)^{1/2}$; σ and μ are electrical conductivity and dynamic viscosity of the fluid, respectively. B_0 is strength of the applied external magnetic field. In this work, we have conducted simulations for Reynolds number Re from 400 to 5000 and the Stuart number N from 0.0 to 2.0. The boundary conditions at the walls are no-penetration and no-slip for momentum and insulated for the current flow.

The above equations are solved with an in-house code, CUFLOW [59–61]. CUFLOW is a general purpose code for simulating laminar and turbulent flows in complex domains. The code employs Cartesian grids to integrate the 3D unsteady incompressible Navier–Stokes equations. The continuity and momentum equations are solved using a fractional step method. Brief details of the solution algorithm are provided below and complete details are available in Refs. [60] and [61].

In the first step of the fractional step method, intermediate velocities are determined by solving the momentum equations without the pressure gradient terms. The discretized equations are derived by a finite-volume framework using central differencing for both convection and diffusion terms on a collocated grid. For the temporal differencing, the second-order accurate Adams–

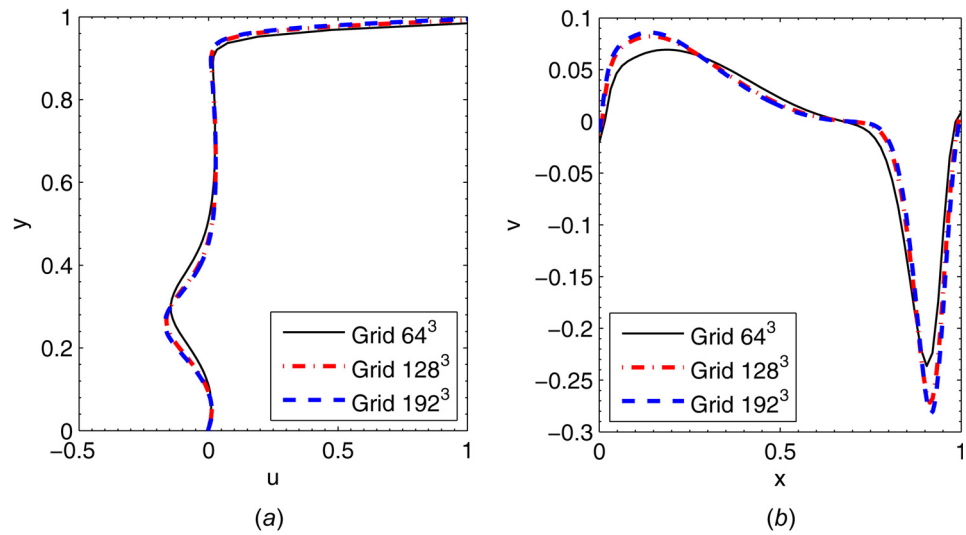

Fig. 3 Grid independency study, Re = 3200 and *N* = 0.25 in symmetry plane (*z* = 0.5)

Downloaded From: http://asmedigitalcollection.asme.org/ on 03/26/2015 Terms of Use: http://asme.org/terms

Table 1 List of all simulations

No.	Re	N	Grid	Steady/unsteady
1	400	0	128^3	Steady
2	400	0.25	128^3	Steady
3	400	0.5	128^3	Steady
4	400	1	128^3	Steady
5	400	2	128^3	Steady
6	2000	0	128^3	Unsteady
7	2000	0.0125	128^3	Unsteady
8	2000	0.05	128^3	Steady
9	2000	0.25	128^3	Steady
10	2000	0.5	128^3	Steady
11	2000	1	128^3	Steady
12	2000	2	128^3	Steady
13	3200	0	128^3	Unsteady
14	3200	0.04	128^3	Unsteady
15	3200	0.0625	128^3	Steady
16	3200	0.09	128^3	Steady
17	3200	0.25	128^3	Steady
18	3200	0.5	128^3	Steady
19	3200	1	128^3	Steady
20	3200	2	128^3	Steady
21	5000	0	192^3	Unsteady
22	5000	0.25	192^3	Steady
23	5000	0.5	192^3	Steady

Bashforth scheme is used. The discretized equations in the absence of pressure gradient terms are given by

$$\rho\left(\frac{\hat{u}_i - u_i^n}{\Delta t}\right) = \frac{3}{2}H_{u_i}^n - \frac{1}{2}H_{u_i}^{n-1} \tag{7}$$

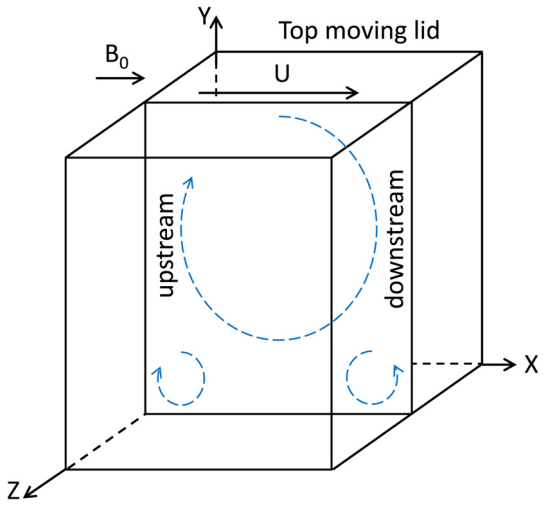

Fig. 4 The lid driven cavity with an external magnetic field

Here, u_i denotes the velocity in the i direction, and u_1 stands for u velocity, u_2 stands for v velocity, and u_3 stands for w velocity. In the second step, the continuity equation is transformed to a pressure-Poisson equation given by

$$\frac{\rho}{\Delta t}\frac{\partial \hat{u}_i}{\partial x_i} = \frac{\partial}{\partial x_i}\left(\frac{\partial p}{\partial x_i}\right)^{n+1} \tag{8}$$

Equation (8) for pressure is solved efficiently by a V-cycle multigrid method and red–black successive over relaxation (SOR) (with over-relaxation parameter of 1.6). After computing the pressure at $n+1$ time step from Eq. (8), the velocity components are

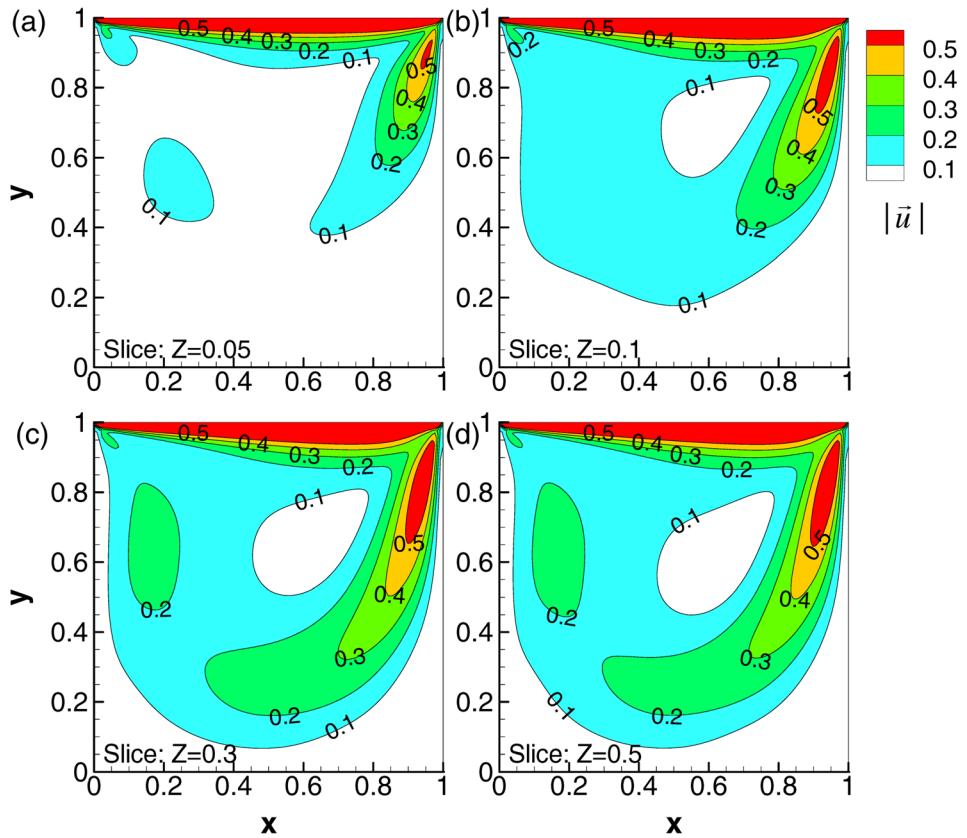

Fig. 5 Velocity magnitude contour at Re = 400 and N = 0.0 on: (*a*) z = 0.05, (*b*) z = 0.1, (*c*) z = 0.3, and (*d*) z = 0.5

Downloaded From: http://asmedigitalcollection.asme.org/ on 03/26/2015 Terms of Use: http://asme.org/terms

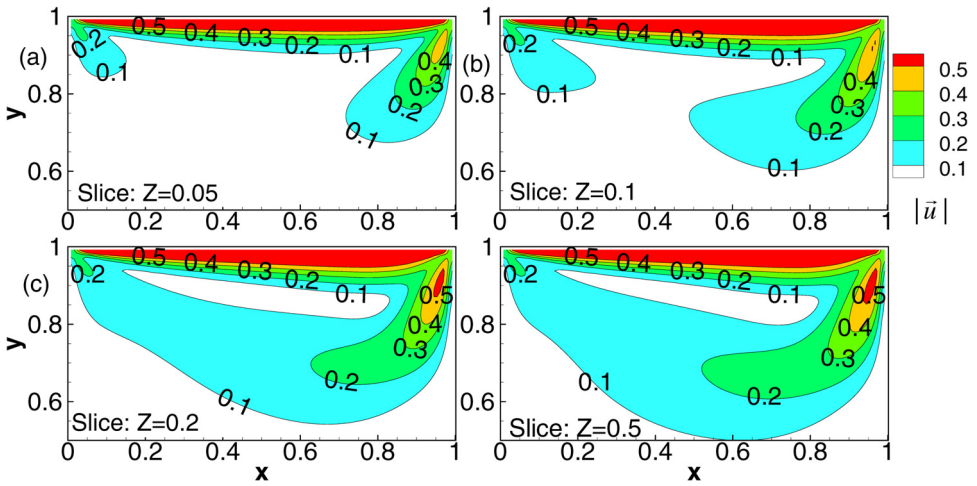

Fig. 6 Velocity magnitude contour at Re = 400 and $N = 1.0$ on: (*a*) $z = 0.05$, (*b*) $z = 0.1$, (*c*) $z = 0.2$, and (*d*) $z = 0.5$

updated for the effects of the pressure gradient term. For steady state calculations, the algorithm is marched in time to desired degree of convergence in time.

The above algorithm has been programmed to run entirely on a GPU. The GPU has been observed to provide a factor upward of 20 speed-ups over a single core CPU. GPU programming can be done in several different languages such as OpenCL, CUDA, and OpenGL. Of these, OpenCL and CUDA are most commonly used. We have implemented the algorithm in CUDA Fortran. CUDA Fortran is supported by the Portland Group (PGI) Fortran compiler. The grid generation, initial conditions, and boundary conditions are first created on CPU and data are then copied to the GPU. For each computational step, a separate GPU kernel is launched. The flow fields from the GPU are copied periodically to the CPU for plotting and interrogation. In the current version of CUFLOW, an unstructured one-dimensional data structure is employed in order to simulate complex geometries. The GPU launches data in blocks of prespecified sizes and each block is assigned to one streaming multiprocessor (SMP). The SMP launches threads which are then assigned to kernels. A kernel is a set of instructions assigned to one thread to be executed independent of other data. Thus, GPU is a data parallel computer, operating same instructions in parallel on multiple data. As mentioned earlier, CUFLOW uses an explicit algorithm for momentum equations and a red–black SOR algorithm for the pressure-Poisson equation. Both these are data parallel algorithms and easily map to a GPU. CUFLOW has been successfully used to perform several large eddy simulation (LES) and direct numerical simulation (DNS) of turbulence such as in circular and triangular ducts, the effects of a microramp on the film cooling effectiveness [61], and flow and heat transfer in the mold region of continuous casters of steel [60]. Details of these results with CUFLOW are given in Refs. [59–61].

3 Code Validation and Grid Independent Study

Previously, CUFLOW was validated in a number of flow problems, including turbulent flow in square ducts [49], MHD flow in channels and ducts [58], continuous casting of steel [60,62], and in film cooling flow with vortex generators [61]. However, the current version of CUFLOW was modified to use a collocated grid (versus a staggered grid in the previous version) and hence was validated again for flow in a driven cube with a Newtonian fluid against the previous simulations of Ku et al. [20]. Figure 1 shows the comparison of the velocity profiles at midspan along horizontal and vertical lines. The solution of Ku et al. [20] was

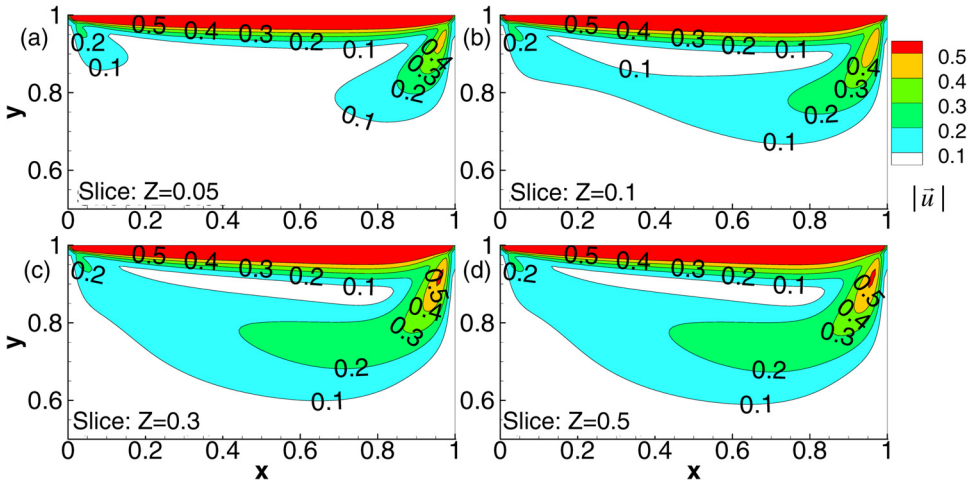

Fig. 7 Velocity magnitude contour at Re = 400 and $N = 2.0$ on: (*a*) $z = 0.05$, (*b*) $z = 0.1$, (*c*) $z = 0.3$, and (*d*) $z = 0.5$

Downloaded From: http://asmedigitalcollection.asme.org/ on 03/26/2015 Terms of Use: http://asme.org/terms

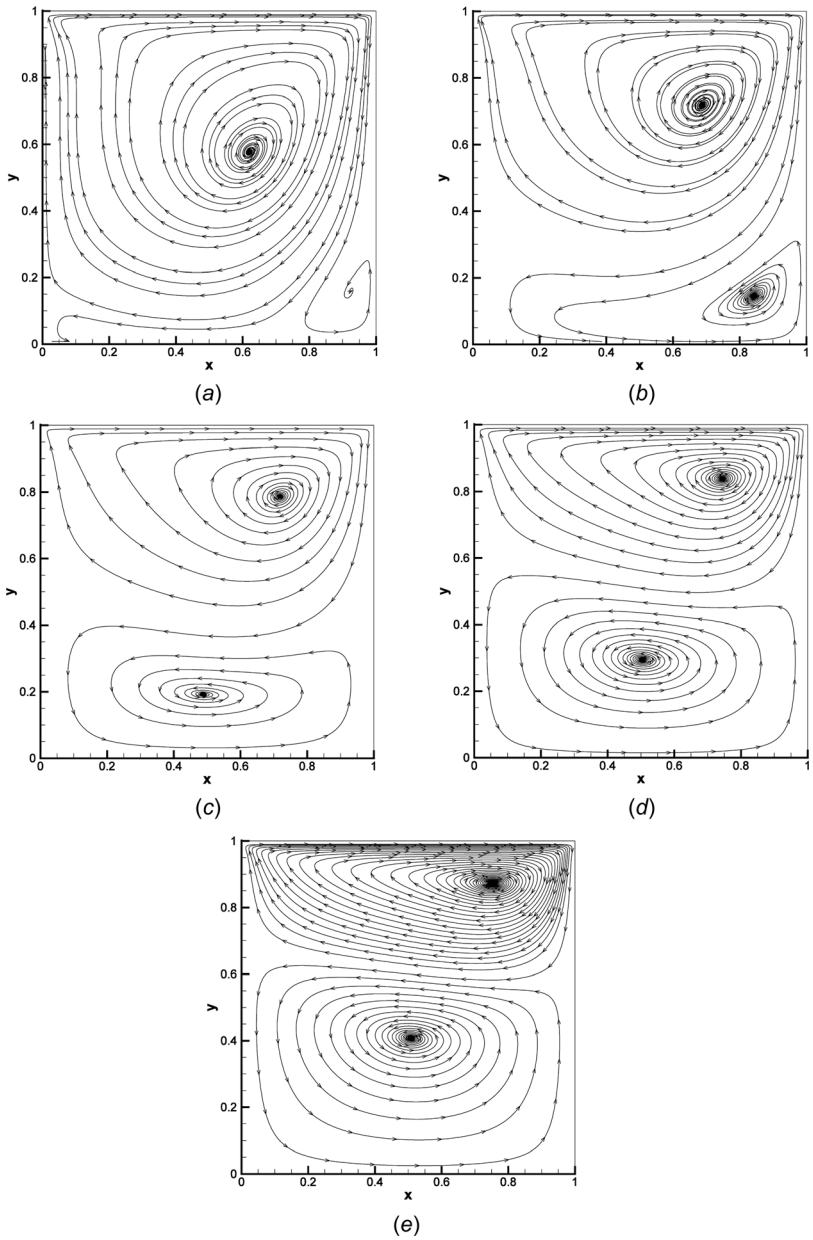

Fig. 8 Streamlines in $z = 0.5$ plane, Re = 400 for different N

obtained with a spectral technique and our simulations were performed with a $128 \times 128 \times 128$ uniform finite volume grid. Several coarser grids were also computed, and the $128 \times 128 \times 128$ was able to match very well with the results from Ku et al. [20]. Since the code used a GPU, the computations were quite fast and did not require much GPU time. The calculations were performed by marching in time to steady state, and a steady state was judged by successive changes of velocities to be less than 1.0×10^{-5} for a nominal value of 1.0.

The validation of the MHD part of the solver was done by solving a lid-driven cavity flow in a cavity of aspect ratio $x{:}y{:}z = 1{:}1{:}8$ with a grid of $128 \times 128 \times 512$ finite volumes for CUFLOW and $128 \times 128 \times 100$ for ANSYS FLUENT [63]. The magnetic field was applied in the x direction and top wall ($y = 1$) was moving in the x direction with velocity of 1.0. The Reynolds number of this problem was 5000 and the Stuart number $N = 5$. A 2D version of this problem, which assumes infinite length in z direction, has been previously reported by Shatrov et al. [54]. In Fig. 2, the u velocities on vertical centerline of the symmetry plane of the 3D simulations are compared with the velocity from the 2D simulation. The agreement between the two is excellent, thus validating the solution of the MHD equations as well. Next, grid independency studies were carried out to establish an adequate grid that gives accurate results.

Calculations were made with $64 \times 64 \times 64$, $128 \times 128 \times 128$, and $192 \times 192 \times 192$ finite volumes for $\mathrm{Re} = 3200$ and $N = 0.25$. The u velocity on vertical centerline in the symmetry plane ($z = 0.5$) and v velocity on the horizontal centerline are plotted in Fig. 3.

These comparisons show that results from $64 \times 64 \times 64$ grid are not accurate enough, but results with $128 \times 128 \times 128$ and $192 \times 192 \times 192$ grids are very close to each other. A little mismatch at the maximum v velocity is seen between the $128 \times 128 \times 128$ and the $192 \times 192 \times 192$ grid. Therefore, in the current study for Reynolds numbers 3200 and less the $128 \times 128 \times 128$ grid is used whereas the $192 \times 192 \times 192$ grid is used for Re of 5000.

Downloaded From: http://asmedigitalcollection.asme.org/ on 03/26/2015 Terms of Use: http://asme.org/terms

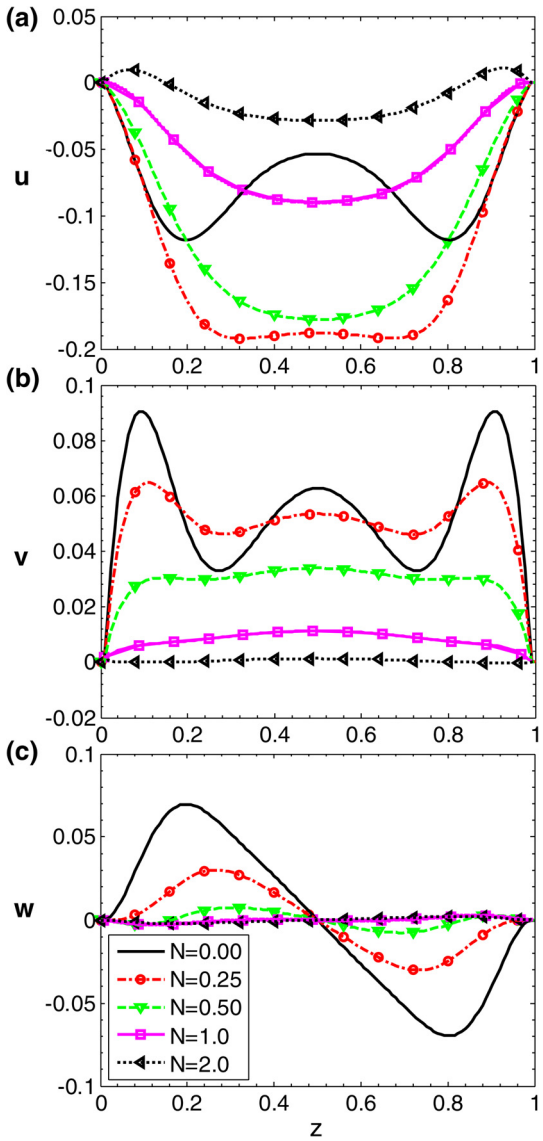

Fig. 9 (*a*) *u*, (*b*) *v*, and (*c*) *w* velocities on spanwise centerline

4 Results and Discussions

In this work, a total of 23 simulations were performed with Reynolds number Re ranging from 400 to 5000 and Stuart number N ranging from 0.0 to 2.0. Table 1 lists the parameters for these computations. The top lid, represented by surface $y = 1$, moves in the x direction with the magnetic field applied in the same direction. Figure 4 shows the geometrical configuration.

4.1 Simulations at Re = 400. Four simulations with different Stuart numbers have been conducted for $\mathrm{Re} = 400$. Due to the low Reynolds number, steady state solutions were obtained for all these cases. Figure 5 shows the contours of velocity magnitude in different constant z planes. The results show that without the magnetic field the primary eddy occupies almost the entire cavity and the velocity contours show that the streamwise behavior at $z = 0.3$ is very similar to that $z = 0.5$ which is the symmetry plane. Figure 6 shows contours of velocity magnitude in different z planes at $N = 1.0$. Comparing these plots with those for $N = 0$, we observe that the main eddy is compressed significantly with the region of velocity magnitude greater than 0.1 (10% of top wall velocity) occupying the top half of the cavity. Increasing N further to 2.0, the recirculating region moves up further and takes around top 40% of the cavity, as shown in Fig. 7.

The streamlines on the middle z plane ($z = 0.5$) are shown in Fig. 8. Figure 8(*a*) shows that with no magnetic field, there is a relatively small secondary eddy at the bottom right corner of the cavity. However, as N increases, the main eddy moves up and this secondary eddy grows. Eventually when N exceeds 0.25, the secondary eddy occupies completely the bottom half of the cavity. However, the velocity in the bottom region of the cavity is very small and the flow is almost stationary for the Stuart number $N \geq 1$. Figure 8(*d*) shows the streamlines for case $\mathrm{Re} = 400$ and $N = 1.00$, and the result shows that in this case the bottom eddy has about equal size as the top main eddy. However, the eye of the bottom eddy is at the center of the bottom half of the cavity, while the eye of the top eddy is close to the downstream corner. It is important to mention that the strength of the secondary eddy is still much smaller than that of the primary eddy. This can also be seen from Fig. 10(*a*) where the u velocity is very small for the region $y < 0.3$.

The u, v, and w velocities on the line passing through the center and between the two side walls are shown in Fig. 9. When no magnetic field is applied, the u velocity shows a "W-like" shape, and u has a negative through the line. As N increases, the main eddy moves up along with the bottom part of the eddy also moving up. This makes the u velocity more negative. With increasing N, this velocity increases (decreasing in magnitude) with even a change in sign near the side walls for $N = 2$. The v velocity along the spanwise centerline is positive for all the different Stuart numbers. When no magnetic field is applied the peak v velocity on the spanwise centerline is seen at region about 0.1 away from the side walls, and has a local peak v velocity at the middle with $z = 0.5$. The results show that as N increases, the v velocity becomes

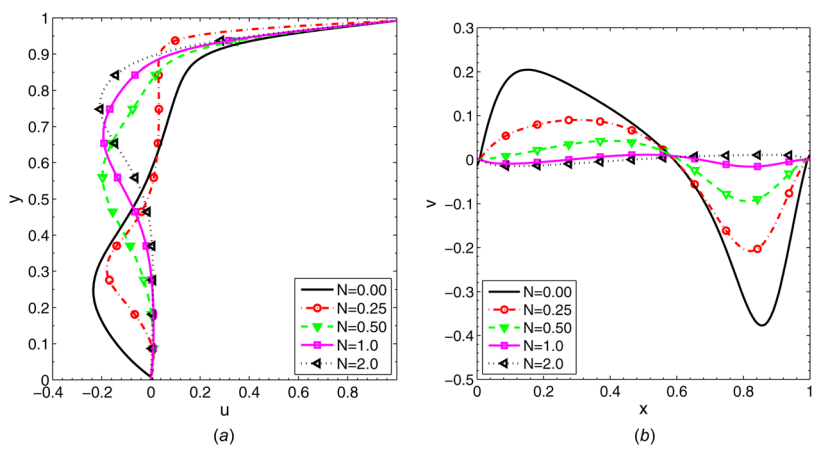

Fig. 10 Centerline velocities in $z = 0.5$ plane, $\mathrm{Re} = 400$ for different magnetic fields

Downloaded From: http://asmedigitalcollection.asme.org/ on 03/26/2015 Terms of Use: http://asme.org/terms

Table 2 Re = 400 *u* velocity on vertical centerline *x* = 0.5

y	*N* = 0.00	*N* = 0.25	*N* = 0.50	*N* = 1.00	*N* = 2.00
0.10	-1.43×10^{-1}	-8.16×10^{-4}	1.06×10^{-2}	1.00×10^{-2}	4.86×10^{-3}
0.20	-2.22×10^{-1}	-8.38×10^{-2}	-1.30×10^{-3}	9.94×10^{-3}	7.15×10^{-3}
0.30	-2.21×10^{-1}	-1.79×10^{-1}	-4.01×10^{-2}	-7.73×10^{-4}	8.08×10^{-3}
0.40	-1.40×10^{-1}	-1.02×10^{-1}	-1.08×10^{-1}	-3.12×10^{-2}	1.04×10^{-3}
0.50	-5.02×10^{-2}	-1.13×10^{-2}	-1.80×10^{-1}	-9.28×10^{-2}	-3.02×10^{-2}
0.60	1.20×10^{-2}	2.12×10^{-2}	-1.91×10^{-1}	-1.65×10^{-1}	-9.58×10^{-2}
0.70	6.20×10^{-2}	3.18×10^{-2}	-1.19×10^{-1}	-1.90×10^{-1}	-1.85×10^{-1}
0.80	1.10×10^{-1}	3.19×10^{-2}	-2.24×10^{-2}	-1.17×10^{-1}	-1.90×10^{-1}
0.90	2.25×10^{-1}	3.56×10^{-2}	1.34×10^{-1}	7.61×10^{-2}	1.94×10^{-2}

Table 3 Re = 400 *v* velocities on horizontal line *y* = 0.5

x	*N* = 0.00	*N* = 0.25	*N* = 0.50	*N* = 1.00	*N* = 2.00
0.10	1.91×10^{-1}	6.00×10^{-2}	9.71×10^{-3}	-9.60×10^{-3}	-1.52×10^{-2}
0.20	1.98×10^{-1}	8.21×10^{-2}	2.36×10^{-2}	-5.71×10^{-3}	-1.32×10^{-2}
0.30	1.62×10^{-1}	9.04×10^{-2}	3.71×10^{-2}	1.23×10^{-3}	-8.69×10^{-3}
0.40	1.16×10^{-1}	8.22×10^{-2}	4.25×10^{-2}	7.79×10^{-3}	-3.50×10^{-3}
0.50	6.04×10^{-2}	5.18×10^{-2}	3.32×10^{-2}	1.09×10^{-2}	1.53×10^{-3}
0.60	-6.45×10^{-3}	-5.70×10^{-3}	3.51×10^{-3}	7.44×10^{-3}	5.44×10^{-3}
0.70	-1.22×10^{-1}	-1.08×10^{-1}	-5.23×10^{-2}	-4.69×10^{-3}	8.31×10^{-3}
0.80	-3.18×10^{-1}	-2.05×10^{-1}	-9.43×10^{-2}	-1.60×10^{-2}	9.82×10^{-3}
0.90	-3.26×10^{-1}	-1.43×10^{-1}	-6.08×10^{-2}	-1.08×10^{-2}	1.06×10^{-2}

smaller and the profile is flatter. The w velocity on the spanwise centerline is plotted in Fig. 9(*c*) which shows a wavy shape for low vales of N. For large N, the w velocity is seen to diminish to nearly a zero value. The peak w velocity happens in the region around $z = 0.2$ away for the case when no magnetic file is applied, and varies linearly between $z = 0.2$ and $z = 0.8$. The results also show that as N increases, the magnitude of w velocity decreases.

Figure 10 shows the u velocity on the vertical centerline and v velocity on the horizontal centerline in the symmetry plane ($z = 0.5$). Selected points on these lines are tabulated in Tables 2 and 3. Figure 10(*a*) shows that as N increases, the negative peak of u velocity shifts upward toward the top moving wall. It also shows that the maximum magnitude of the negative u velocity is only slightly affected by increasing N, so applying the magnetic field only shifts the negative peak u velocity from bottom of the cavity to a region closer to the top moving wall. It also shows with $N \geq 1$, the bottom half of the cavity is almost stationary and the primary eddy is confined in the top half of the cavity. Figure 10(*b*) shows the v velocity on horizontal centerline. It is seen that the peak of v velocity decreases with increasing N, and as N increases from 0 to 1, the negative peak value is reduced from -0.38 to -0.016. This is a result of the suppression of flow circulation and shifting of the center of flow upwards due to the magnetic field. Because the magnetic field is applied in the x direction, and the damping effect is mainly in the y direction.

4.2 Simulations at Re = 2000. Increasing the Reynolds number increases the nonlinearity and strength of the advection terms. The Re = 2000 simulations were also performed with a 128^3 grid. Figure 11 shows the streamlines on the symmetry plane ($z = 0.5$) for several values of N. We observe that when there is no magnetic field or when only a weak magnetic field ($N = 0.0125$) is applied, the flow is unsteady. Therefore, the lines in the plots are instantaneous streaklines obtained by releasing massless tracing particles on a typical frozen instantaneous flow field. For $N = 0$, Fig. 11 shows that without the magnetic field, there are two small secondary eddies located at the bottom corners. After applying a modest magnetic field, with $N = 0.05$, there are still two secondary eddies at the bottom corners, but the flow is steady for this Stuart number and higher. Comparing the six plots shown in Fig. 11, we see that with increasing N, the main eddy moves upward and toward the top downstream corner of the cavity. This trend is similar to the 2D cases described in Refs. [51] and [52]. Comparing the shape of the primary eddy for different values of N, it is seen that the shape of the primary eddy also changes from a circular shape to an elliptic shape similar to the 2D case reported by Ref. [54].

Figure 11(*c*) shows the streamlines in the central z plane for Re = 2000 and $N = 0.25$. In this case, also the flow is steady with two secondary eddies still seen at the bottom of the cavity. However, there is a trend toward the two secondary eddies to interact with each other and merge into a bigger one. This is seen with increasing N further to 0.5. Figure 11(*d*) for $N = 0.5$ shows that the two bottom secondary eddies form a large eddy that occupies the bottom of the cavity. As N is further increased to 1.0, the top main eddy shrinks and bottom eddy grows even larger than the primary eddy. But the strength of the bottom eddy is much smaller than the primary one. Eventually, when $N = 2.0$ the main eddy shrinks to the very top of the cavity and only occupies top one-third of the cavity as shown in Fig. 11(*f*). In this case, secondary and weak tertiary eddies start to appear in the bottom part of the cavity.

The u velocity on vertical centerlines and v velocity on horizontal centerline for $z = 0.5$ are shown in Fig. 12. For different N, Fig. 12(*a*) illustrates that with increasing N the peak of u is moving away from the bottom wall and the bottom wall boundary layer thickness is growing. As the peak moving away from the wall, the peak value remains almost the same and is not affected considerably. Figure 12(*a*) shows that when $N = 2.00$, the flow field below $y = 0.5$ is almost stationary. The main effect of increasing N on u is the shift in the peak u velocity towards the moving lid. Figure 12(*b*) illustrates that increasing N, the peak v velocity is reduced and the boundary layer that adjacent to the sidewall becomes thicker. The growth of the boundary layer pushes the peak v velocity away from the side walls. Selected points in Figs. 12(*a*) and 12(*b*) are tabulated in Tables 4 and 5, respectively.

Figure 13 shows velocity vectors in the middle x plane ($x = 0.5$). As seen in Fig. 13(*a*), when there is no magnetic field, four vortices (TGL vortex pairs) are seen at the four corners, and the two vortices at the bottom are much stronger than those in the upper region. However, for $N = 1.0$, these four vortices disappear as a results of the damping effect of the magnetic field.

Downloaded From: http://asmedigitalcollection.asme.org/ on 03/26/2015 Terms of Use: http://asme.org/terms

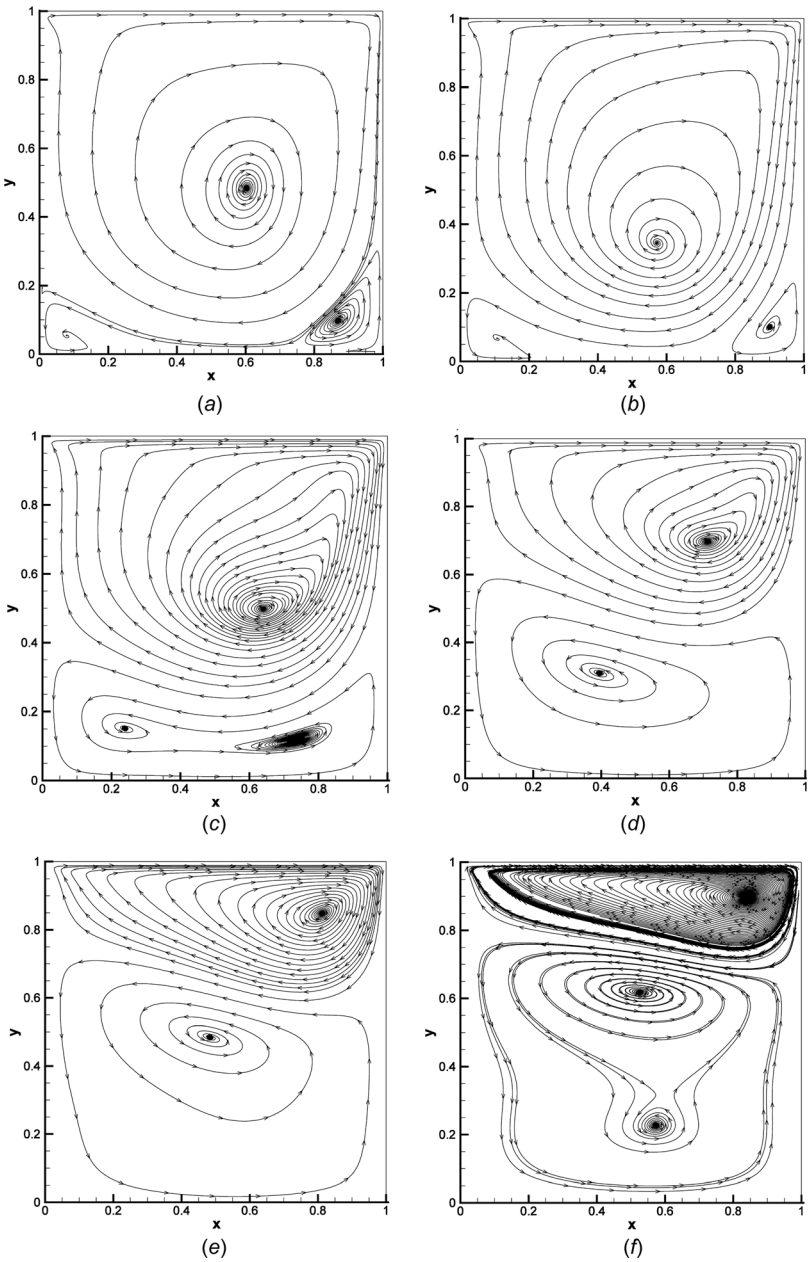

Fig. 11 Streamlines in $z = 0.5$ plane, Re = 2000 for different N

4.3 Simulations at Re = 3200. Further increase of Re to 3200 makes the flow more nonlinear and the flow is seen to be unsteady for $N = 0$ and $N = 0.04$. Figures 14(*a*) and 14(*b*) show the instantaneous streakline plot of the flow fields generated with $N = 0$ and $N = 0.04$. Increase of N to 0.0625 makes the flow steady, as shown in Fig. 14(*c*). It is seen that for $N = 0.04$ and $N = 0.0625$, the eye of the primary vortex moves down below the position seen for $N = 0$. At $N = 0.0625$, two secondary eddies are formed at the bottom corner of the cavity. Similar streamline pattern is seen for $N = 0.09$. Further increase of the magnetic interaction parameter shrinks the top circulation eddy and modifies the shape of the eddy from a circular to elliptical, as seen also for Re = 2000. The general flow patterns observed until $N = 2.0$ are similar to those seen at Re = 2000. The bottom two secondary eddies seen at $N = 0.25$ merge into a single large secondary eddy in Fig. 14(*f*) at $N = 0.5$. At $N = 1.0$ and 2.0, the primary eddy shrinks and only occupies the top one-third of the cavity. Below the primary eddy, one secondary and one tertiary eddy show up. However, these two eddies are much weaker that the primary one.

Figure 15 shows the u velocity on vertical centerline and v velocity on horizontal centerline on the symmetry plane for Re = 3200, and again selected points are tabulated in Tables 6 and 7, respectively. As seen before, Fig. 15(*a*) shows that the location of the peak u velocity is shifted upward (since the main eddy moves upward) with increasing N, but its magnitude is only slightly decreased. Figure 15(*b*) shows that the v velocity on horizontal centerline is suppressed with increasing N, and the boundary layer grows accordingly.

The velocity vectors in the central x plane ($x = 0.5$) are plotted in Figs. 16(*a*) and 16(*b*) for the cases $N = 0$ and $N = 0.5$, respectively. Figure 16(*a*) shows without the magnetic field, four vortex pairs are found at the bottom of the cavity and two vortices appears on the two top corners. These TGL vortex pairs have also been found by other researchers [21]. Figure 16(*b*) shows that when the magnetic field is increased to $N = 0.5$ all these bottom wall vortices disappear. This is obviously a result of suppressing the lower circulation in the bottom portion of the cavity.

Downloaded From: http://asmedigitalcollection.asme.org/ on 03/26/2015 Terms of Use: http://asme.org/terms

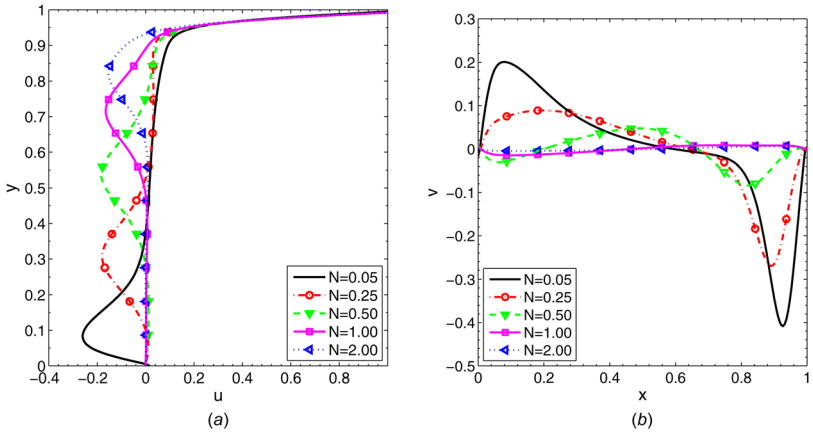

Fig. 12 Centerline velocity in $z = 0.5$ plane, Re = 2000

Table 4 Re = 2000 *u* velocity on vertical centerline $x = 0.5$

Y	$N = 0.25$	$N = 0.50$	$N = 1.00$	$N = 2.00$
0.10	-8.16×10^{-4}	1.12×10^{-2}	2.47×10^{-3}	1.54×10^{-3}
0.20	-8.38×10^{-2}	1.13×10^{-2}	2.39×10^{-3}	3.06×10^{-4}
0.30	-1.79×10^{-1}	-4.69×10^{-3}	4.68×10^{-3}	-1.70×10^{-4}
0.40	-1.02×10^{-1}	-6.06×10^{-2}	7.27×10^{-3}	2.29×10^{-3}
0.50	-1.13×10^{-2}	-1.70×10^{-1}	-6.20×10^{-3}	8.04×10^{-3}
0.60	2.12×10^{-2}	-1.43×10^{-1}	-6.47×10^{-2}	5.23×10^{-3}
0.70	3.18×10^{-2}	-3.18×10^{-2}	-1.62×10^{-1}	-4.62×10^{-2}
0.80	3.19×10^{-2}	1.90×10^{-2}	-9.52×10^{-2}	-1.48×10^{-1}
0.90	3.56×10^{-2}	4.71×10^{-2}	8.07×10^{-3}	-8.62×10^{-2}

Table 5 Re = 2000 *v* velocity on horizontal line $y = 0.5$

x	$N = 0.25$	$N = 0.50$	$N = 1.00$	$N = 2.00$
0.10	7.88×10^{-2}	-2.55×10^{-2}	-1.50×10^{-2}	-4.85×10^{-3}
0.20	8.89×10^{-2}	-1.25×10^{-3}	-1.27×10^{-2}	-4.48×10^{-3}
0.30	7.94×10^{-2}	2.26×10^{-2}	-8.47×10^{-3}	-3.74×10^{-3}
0.40	5.63×10^{-2}	4.06×10^{-2}	-3.48×10^{-3}	-2.67×10^{-3}
0.50	2.91×10^{-2}	4.71×10^{-2}	1.75×10^{-3}	-1.21×10^{-3}
0.60	7.72×10^{-3}	3.12×10^{-2}	5.99×10^{-3}	5.15×10^{-4}
0.70	-1.16×10^{-2}	-2.00×10^{-2}	8.23×10^{-3}	2.73×10^{-3}
0.80	-9.47×10^{-2}	-8.18×10^{-2}	7.89×10^{-3}	4.93×10^{-3}
0.90	-2.68×10^{-1}	-4.04×10^{-2}	7.90×10^{-3}	6.37×10^{-3}

4.4 Simulations at Re = 5000. We finally consider an even higher Re of 5000. For this high Reynolds number, we have used a 192^3 grid and integrated the equations in time with high accuracy at each time step. For $N = 0$, the flow is unsteady. Steady solutions are obtained for $N = 0.25$ and higher. Figures 17(*a*) and 17(*b*) show the streaklines for $N = 0.25$ and $N = 0.5$. Since the qualitative features seen here are similar to those for Re = 3200 and Re = 2000, results for higher N were not computed.

The (x, y) coordinates of the eye of the primary eddy in the symmetry plane ($z = 0.5$) for all Reynolds numbers are tabulated in Table 8 with different Stuart numbers. As seen in earlier plots with increasing strength of the magnetic field, the center of the primary eddy moves toward the top lid and the downstream corner (top and right corner). One may also notice that for $N = 2$, with increasing Reynolds number, the eye of the primary eddy is closer to the right top corner (top and downstream side) of the cavity. For fixed Re, with increasing N, the path of the eye of the main eddies are nearly on a straight line. The upward motion of the eye of the main eddy is a result of the damping effect of the applied magnetic field.

5 Summary

In this paper, we have studied the flow of an electrically conducting fluid in a 3D cavity subjected to a magnetic field. The time-dependent Navier–Stokes equations are integrated with a second-order accurate numerical scheme and a very fine grid. The code is parallelized on a GPU for computational efficiency. The general features observed for the case of no magnetic field are in agreement with the previous computational and experimental

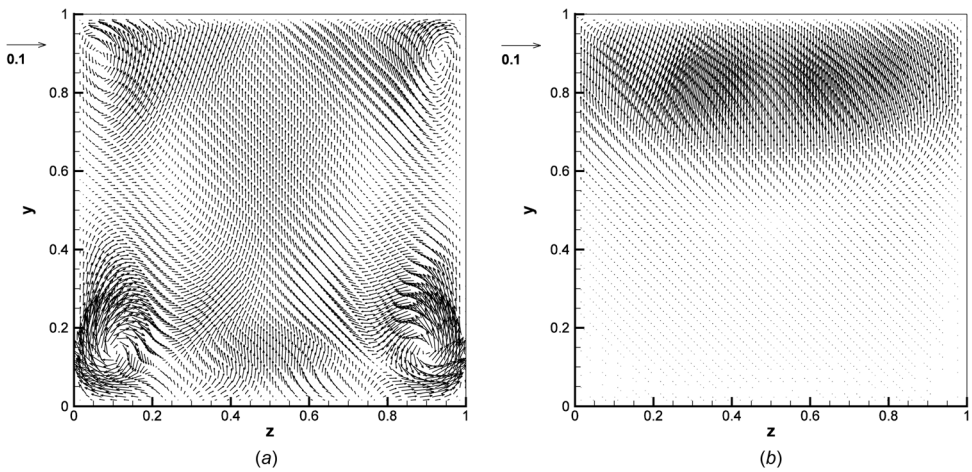

Fig. 13 Velocity vector in middle *x* plane for Re = 2000

Downloaded From: http://asmedigitalcollection.asme.org/ on 03/26/2015 Terms of Use: http://asme.org/terms

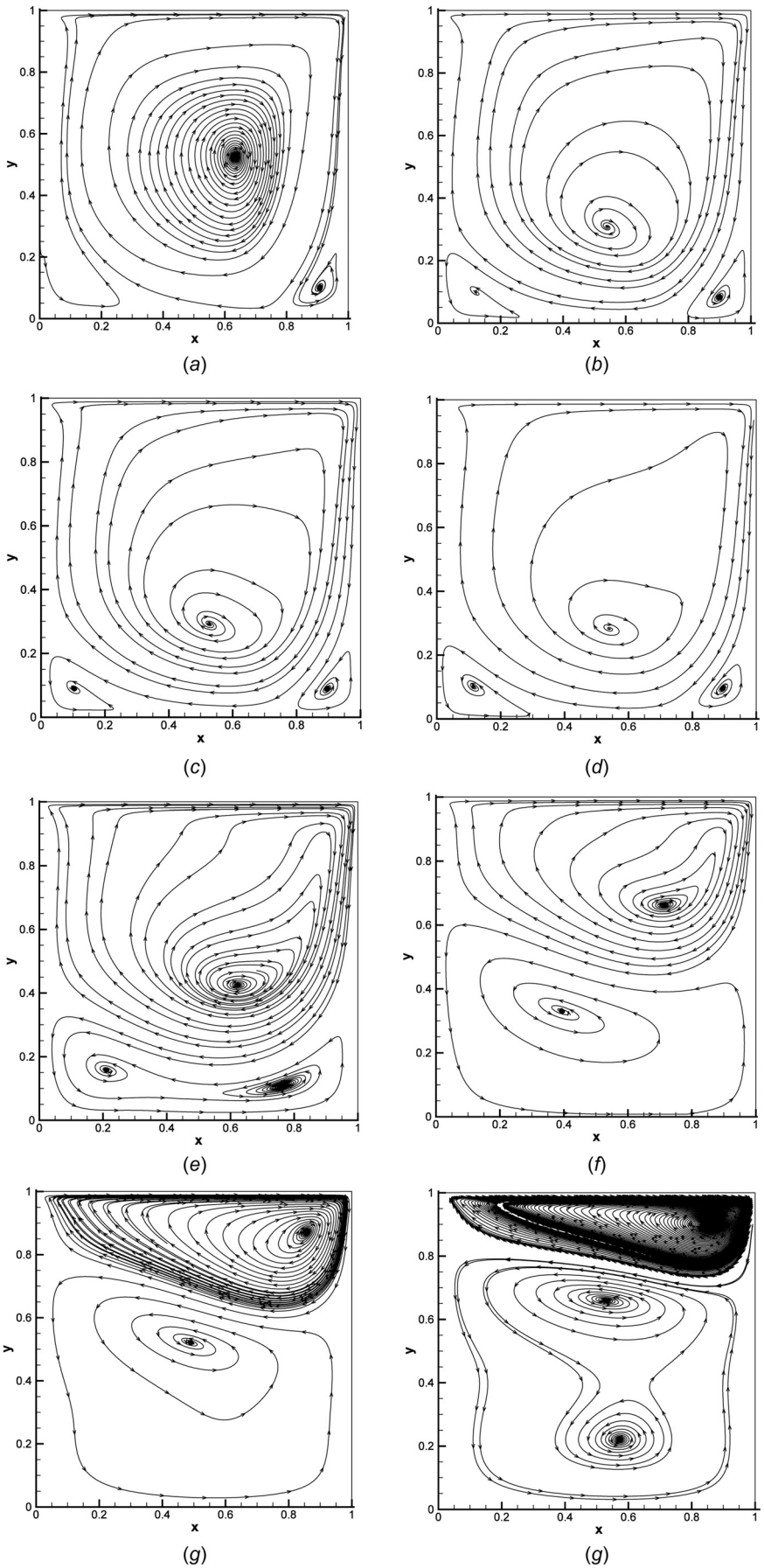

Fig. 14 Streamlines in $z = 0.5$ plane, Re = 3200 for different N

Downloaded From: http://asmedigitalcollection.asme.org/ on 03/26/2015 Terms of Use: http://asme.org/terms

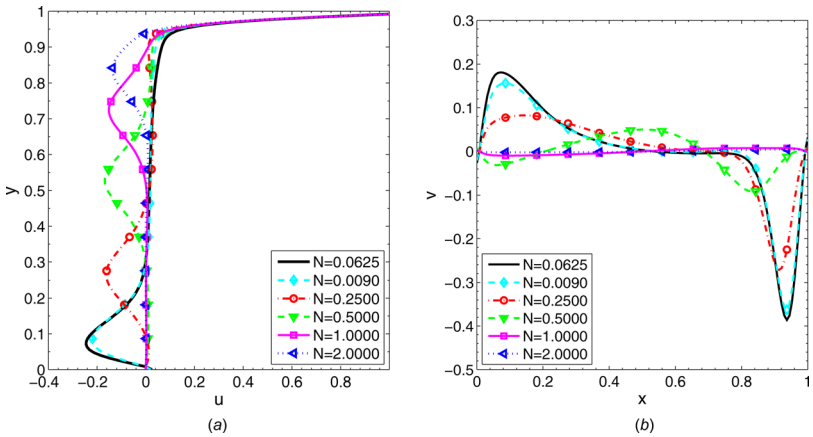

Fig. 15 Centerline velocity in $z = 0.5$ plane, Re = 3200

Table 6 Re = 3200 *u* velocity on vertical centerline $x = 0.5$

y	$N = 0.25$	$N = 0.50$	$N = 1.00$	$N = 2.00$
0.10	-5.54×10^{-3}	8.78×10^{-3}	2.34×10^{-3}	1.38×10^{-3}
0.20	-1.18×10^{-1}	8.84×10^{-3}	9.28×10^{-4}	1.57×10^{-4}
0.30	-1.47×10^{-1}	-1.07×10^{-3}	1.69×10^{-3}	-4.96×10^{-4}
0.40	-3.62×10^{-2}	-4.88×10^{-2}	5.47×10^{-3}	1.97×10^{-4}
0.50	1.37×10^{-2}	-1.60×10^{-1}	2.46×10^{-3}	4.44×10^{-3}
0.60	2.65×10^{-2}	-1.08×10^{-1}	-3.70×10^{-2}	8.66×10^{-3}
0.70	2.73×10^{-2}	-1.09×10^{-2}	-1.43×10^{-1}	-1.65×10^{-2}
0.80	2.05×10^{-2}	1.87×10^{-2}	-8.44×10^{-2}	-1.20×10^{-1}
0.90	1.11×10^{-2}	2.81×10^{-2}	8.30×10^{-3}	-8.60×10^{-2}

Table 7 Re = 3200 *v* velocity on horizontal line $y = 0.5$

X	$N = 0.25$	$N = 0.50$	$N = 1.00$	$N = 2.00$
0.10	7.97×10^{-2}	-2.62×10^{-2}	-1.02×10^{-2}	-2.57×10^{-3}
0.20	7.75×10^{-2}	-7.82×10^{-4}	-8.87×10^{-3}	-2.42×10^{-3}
0.30	5.85×10^{-2}	2.05×10^{-2}	-6.79×10^{-3}	-2.16×10^{-3}
0.40	3.50×10^{-2}	3.98×10^{-2}	-3.87×10^{-3}	-1.69×10^{-3}
0.50	1.58×10^{-2}	4.99×10^{-2}	-3.07×10^{-4}	-9.25×10^{-4}
0.60	4.74×10^{-3}	3.78×10^{-2}	3.23×10^{-3}	1.20×10^{-4}
0.70	-3.10×10^{-4}	-8.56×10^{-3}	6.15×10^{-3}	1.59×10^{-3}
0.80	-2.58×10^{-2}	-8.28×10^{-2}	7.10×10^{-3}	3.14×10^{-3}
0.90	-2.50×10^{-1}	-4.85×10^{-2}	7.25×10^{-3}	4.15×10^{-3}

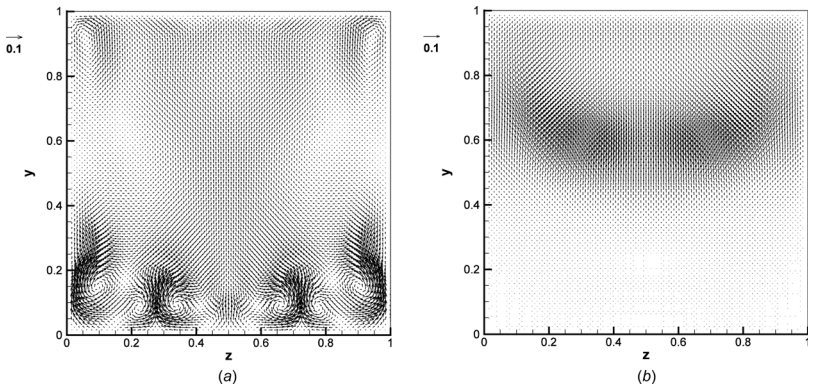

Fig. 16 Velocity vector in middle *x* plane for Re = 3200

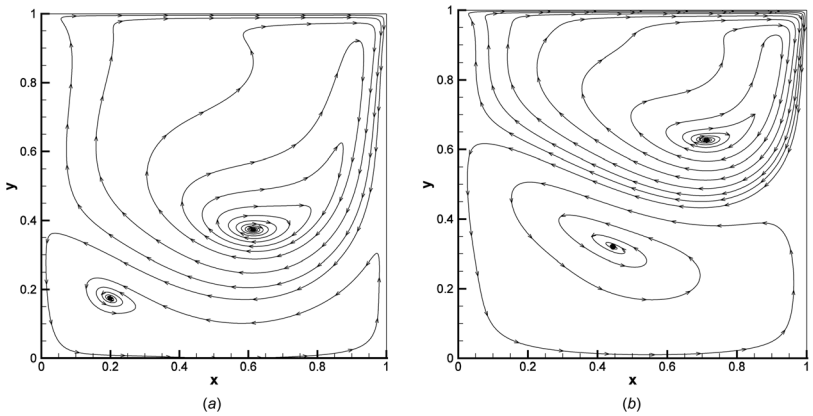

Fig. 17 Streamlines in $z = 0.5$ plane, Re = 5000 for $N = 0.25$ and $N = 0.50$

Downloaded From: http://asmedigitalcollection.asme.org/ on 03/26/2015 Terms of Use: http://asme.org/terms

Table 8 (x, y) coordinates of the eye of the primary eddy in $z = 0.5$ plane

N	Re = 400		Re = 2000		Re = 3200		Re = 5000	
	x	y	x	y	x	y	X	y
0	0.622	0.577	0.603	0.484	0.633	0.523	–	–
0.25	0.688	0.719	0.641	0.499	0.622	0.425	0.613	0.373
0.5	0.719	0.786	0.713	0.696	0.715	0.662	0.712	0.627
1	0.744	0.838	0.812	0.848	0.855	0.871	Not computed	
2	0.753	0.872	0.84	0.896	0.862	0.904	Not computed	

studies. The 3D simulations showed more flow structures including the growth of boundary layers from the side walls. The flow field parallel and close to the side walls is different from the flow in the symmetry plane due to the effect of the side walls. However, the flow behavior in the plane $z = 0.3$ is very similar to the flow field in the symmetry plane ($z = 0.5$). A unique aspect of 3D simulations is the prediction of the formation of TGL vortices in the spanwise direction. The applied external magnetic field is seen to suppress and delay the formation of these TGL vortices. With the magnetic fields, the flow fields are considerably modified as the magnetic field induced force brakes the momentum from the top wall shear. The main recirculating eddy is seen to shrink in size with the formation of a low-velocity region in the lower region of the cavity. With increasing value of the interaction parameter (N), the flow in the lower region of the cavity is nearly suppressed. Further, with a magnetic field, a nominally unsteady flow is stabilized and becomes steady. This paper presents the flow patterns and velocity profiles for 23 runs made at different Reynolds numbers and interaction parameters. We also provide tables of selected profiles of velocities for readers to benchmark their numerical/experimental results for the same parameters.

Acknowledgment

The authors thank the financial supports from the National Science Foundation (Grant No. CMMI 11-30882) and the Continuous Casting Consortium, University of Illinois at Urbana-Champaign, IL. This research is also part of the Blue Waters sustained-petascale computing project, which was supported by the National Science Foundation (Award Nos. OCI-0725070 and ACI-1238993) and the State of Illinois. Blue Waters is a joint effort of the University of Illinois at Urbana-Champaign and its National Center for Supercomputing Applications. The authors also thank NVIDIA Hardware Grant Program for providing GPUs.

References

[1] Ghia, U., Ghia, K. N., and Shin, C., 1982, "High-Resolutions for Incompressible Flow Using the Navier–Stokes Equations and a Multigrid Method," J. Comput. Phys., **48**(3), pp. 387–411.
[2] Gupta, M., Manohar, R. P., and Stephenson, J. W., 1982, "High Order Finite Difference Method for Fluid Flow Problems," 10th IMACS World Congress on System Simulation and Scientific Computation, International Association for Mathematics and Computers in Simulation, pp. 212–214.
[3] Perić, M., Kessler, R., and Scheuerer, G., 1988, "Comparison of Finite-Volume Numerical Methods With Staggered and Colocated Grids," Comput. Fluids, **16**(4), pp. 389–403.
[4] Kondo, N., Tosaka, N., and Nishimura, T., 1991, "Third-Order Upwind Finite Element Formulations for Incompressible Viscous Flow Problems," Comput. Methods Appl. Mech. Eng., **93**(2), pp. 169–187.
[5] Huser, A., and Biringen, S., 1992, "Calculation of Two-Dimensional Shear-Driven Cavity Flows at High Reynolds Numbers," Int. J. Numer. Methods Fluids, **14**(9), pp. 1087–1109.
[6] Sundaresan, S., Nagarajan, S., Deshpande, S., and Narasimha, R., 1998, "2D Lid-Driven Cavity Flow at High Reynolds Numbers: Some Interesting Fluid-Dynamical Issues," 16th International Conference on Numerical Methods in Fluid Dynamics, Archon, France, July 6–10, pp. 231–236.
[7] Aydin, M., and Fenner, R., 2001, "Boundary Element Analysis of Driven Cavity Flow for Low and Moderate Reynolds Numbers," Int. J. Numer. Methods Fluids, **37**(1), pp. 45–64.
[8] Sahin, M., and Owens, R. G., 2003, "A Novel Fully Implicit Finite Volume Method Applied to the Lid-Driven Cavity Problem. Part I: High Reynolds Number Flow Calculations," Int. J. Numer. Methods Fluids, **42**(1), pp. 57–77.
[9] Zhang, J., 2003, "Numerical Simulation of 2D Square Driven Cavity Using Fourth-Order Compact Finite Difference Schemes," Comput. Math. Appl., **45**(1), pp. 43–52.
[10] Bruneau, C.-H., and Saad, M., 2006, "The 2D Lid-Driven Cavity Problem Revisited," Comput. Fluids, **35**(3), pp. 326–348.
[11] Pasquim, B., and Mariani, V., 2008, "Solutions for Incompressible Viscous Flow in a Triangular Cavity Using Cartesian Grid Method," Comput. Model. Eng. Sci., **35**(2), pp. 113–132.
[12] Heaton, C., 2008, "On the Appearance of Moffatt Eddies in Viscous Cavity Flow as the Aspect Ratio Varies," Phys. Fluids (1994–present), **20**(10), p. 103102.
[13] Kalita, J. C., and Gupta, M. M., 2010, "A Streamfunction–Velocity Approach for 2D Transient Incompressible Viscous Flows," Int. J. Numer. Methods Fluids, **62**(3), pp. 237–266.
[14] Patil, D., Lakshmisha, K., and Rogg, B., 2006, "Lattice Boltzmann Simulation of Lid-Driven Flow in Deep Cavities," Comput. Fluids, **35**(10), pp. 1116–1125.
[15] Bustamante, C., Florez, W., Power, H., Giraldo, M., and Hill, A., 2011, "Control Volume-Radial Basis Function Solution of 2D Driven Cavity Flow in Terms of the Velocity Vorticity Formulation," Comput. Model. Eng. Sci., **79**(2), pp. 103–129.
[16] Guo, X., Zhong, C., Zhuo, C., and Cao, J., 2014, "Multiple-Relaxation-Time Lattice Boltzmann Method for Study of Two-Lid-Driven Cavity Flow Solution Multiplicity," Theor. Comput. Fluid Dyn., **28**(2), pp. 215–231.
[17] Backx, E., and Wirz, H. J., 1975, "Numerical Solution of the Navier–Stokes Equations for a 3-D Driven Cavity Flow," GAMM Conference on Numerical Methods in Fluid Mechanics, pp. 7–14.
[18] Freitas, C. J., Street, R. L., Findikakis, A. N., and Koseff, J. R., 1985, "Numerical Simulation of Three-Dimensional Flow in a Cavity," Int. J. Numer. Methods Fluids, **5**(6), pp. 561–575.
[19] Koseff, J., and Street, R., 1984, "The Lid-Driven Cavity Flow: A Synthesis of Qualitative and Quantitative Observations," ASME J. Fluids Eng., **106**(4), pp. 390–398.
[20] Ku, H. C., Hirsh, R. S., and Taylor, T. D., 1987, "A Pseudospectral Method for Solution of the Three-Dimensional Incompressible Navier–Stokes Equations," J. Comput. Phys., **70**(2), pp. 439–462.
[21] Iwatsu, R., Ishii, K., Kawamura, T., Kuwahara, K., and Hyun, J. M., 1989, "Numerical Simulation of Three-Dimensional Flow Structure in a Driven Cavity," Fluid Dyn. Res., **5**(3), pp. 173.
[22] Huang, Y., Ghia, U., Osswald, G., and Ghia, K., 1992, "Velocity-Vorticity Simulation of Unsteady 3-D Viscous Flow Within a Driven Cavity," in *Numerical Simulation of 3-D Incompressible Unsteady Viscous Laminar Flows*, Springer Berlin, pp. 54–66.
[23] Arnal, M., Lauer, O., Lilek, Ž., and Perić, M., 1992, "Prediction of Three-Dimensional Unsteady Lid-Driven Cavity Flow," in *Numerical Simulation of 3-D Incompressible Unsteady Viscous Laminar Flows*, Springer, Berlin, pp. 13–24.
[24] Cantaloube, B., and Le, T., 1992, "Direct Simulation of Unsteady Flow in a Three-Dimensional Lid-Driven Cavity," in *Numerical Simulation of 3-D Incompressible Unsteady Viscous Laminar Flows*, Springer, Berlin, pp. 25–33.
[25] Deshpande, M. D., and Shankar, P. N., 1993, "Structure of Laminar Flow in a Three-Dimensional Driven Cavity," Proceedings of the Fluid Dynamics Symposium in Honour of Professor R. Narasimha on his 60th Birthday, Proceedings of the Fluid Dynamics Symposium, pp. 25–36.
[26] Jordan, S., and Ragab, S., 1994, "On the Unsteady and Turbulent Characteristics of the Three-Dimensional Shear-Driven Cavity Flow," ASME J. Fluids Eng., **116**(3), pp. 439–449.
[27] Cortes, A., and Miller, J., 1994, "Numerical Experiments With the Lid Driven Cavity Flow Problem," Comput. Fluids, **23**(8), pp. 1005–1027.
[28] Yeckel, A., Smith, J. W., and Derby, J. J., 1997, "Parallel Finite Element Calculation of Flow in a Three-Dimensional Lid-Driven Cavity Using the CM-5 and T3D," Int. J. Numer. Methods Fluids, **24**(12), pp. 1449–1461.
[29] Albensoeder, S., Kuhlmann, H., and Rath, H., 2001, "Three-Dimensional Centrifugal-Flow Instabilities in the Lid-Driven-Cavity Problem," Phys. Fluids (1994–present), **13**(1), pp. 121–135.
[30] Guermond, J.-L., Migeon, C., Pineau, G., and Quartapelle, L., 2002, "Start-Up Flows in a Three-Dimensional Rectangular Driven Cavity of Aspect Ratio 1:1:2 at Re = 1000," J. Fluid Mech., **450**, pp. 169–199.
[31] Sheu, T. W., and Tsai, S., 2002, "Flow Topology in a Steady Three-Dimensional Lid-Driven Cavity," Comput. Fluids, **31**(8), pp. 911–934.
[32] Albensoeder, S., and Kuhlmann, H. C., 2005, "Accurate Three-Dimensional Lid-Driven Cavity Flow," J. Comput. Phys., **206**(2), pp. 536–558.
[33] De, S., Nagendra, K., and Lakshmisha, K., 2009, "Simulation of Laminar Flow in a Three-Dimensional Lid-Driven Cavity by Lattice Boltzmann Method," Int. J. Numer. Methods Heat Fluid Flow, **19**(6), pp. 790–815.

Downloaded From: http://asmedigitalcollection.asme.org/ on 03/26/2015 Terms of Use: http://asme.org/terms

[34] Yau, Y., Badarudin, A., and Rubini, P., 2012, "A Numerical Study of Secondary Flow and Large Eddies in a Driven Cavity," J. Mech. Sci. Technol., **26**(1), pp. 93–102.
[35] Siegmann-Hegerfeld, T., Albensoeder, S., and Kuhlmann, H. C., 2013, "Three-Dimensional Flow in a Lid-Driven Cavity With Width-to-Height Ratio of 1.6," Exp. Fluids, **54**(6), pp. 1–9.
[36] Tang, X., Su, Y., Wang, F., and Li, L., 2013, "Numerical Research on Lid-Driven Cavity Flows Using a Three-Dimensional Lattice Boltzmann Model on Non-Uniform Meshes," Sci. China Technol. Sci., **56**(9), pp. 2178–2187.
[37] Dong, D. B., Shi, S. J., Hou, Z. X., and Chen, W. S., 2014, "Numerical Simulation of Viscous Flow in a 3D Lid-Driven Cavity Using Lattice Boltzmann Method," Appl. Mech. Mater., **444**, pp. 395–399.
[38] Verstappen, R., Wissink, J., Cazemier, W., and Veldman, A., 1994, "Direct Numerical Simulations of Turbulent Flow in a Driven Cavity," Future Gener. Comput. Syst., **10**(2), pp. 345–350.
[39] Deshpande, M., and Milton, S. G., 1998, "Kolmogorov Scales in a Driven Cavity Flow," Fluid Dyn. Res., **22**(6), pp. 359–381.
[40] Leriche, E., Gavrilakis, S., and Labrosse, G., 2000, "Direct Numerical Simulation of Lid-Driven Cavity Flow Within a 3D Inhomogeneous Domain on an NEC-SX4 Supercomputer," International Conference on Applications of High-Performance Computing in Engineering, pp. 359–369.
[41] Yao, H., Cooper, R., and Raghunathan, S., 2004, "Numerical Simulation of Incompressible Laminar Flow Over Three-Dimensional Rectangular Cavities," ASME J. Fluids Eng., **126**(6), pp. 919–927.
[42] Paramane, S. B., and Sharma, A., 2008, "Consistent Implementation and Comparison of FOU, CD, SOU, and QUICK Convection Schemes on Square, Skew, Trapezoidal, and Triangular Lid-Driven Cavity Flow," Numer. Heat Transfer B, **54**(1), pp. 84–102.
[43] De Vicente, J., Rodríguez, D., Theofilis, V., and Valero, E., 2011, "Stability Analysis in Spanwise-Periodic Double-Sided Lid-Driven Cavity Flows With Complex Cross-Sectional Profiles," Comput. Fluids, **43**(1), pp. 143–153.
[44] Darr, J. H., and Vanka, S. P., 1991, "Separated Flow in a Driven Trapezoidal Cavity," Phys. Fluids A: Fluid Dyn. (1989–1993), **3**(3), pp. 385–392.
[45] Jyotsna, R., and Vanka, S. P., 1995, "Multigrid Calculation of Steady, Viscous Flow in a Triangular Cavity," J. Comput. Phys., **122**(1), pp. 107–117.
[46] González, L., Ahmed, M., Kühnen, J., Kuhlmann, H. C., and Theofilis, V., 2011, "Three-Dimensional Flow Instability in a Lid-Driven Isosceles Triangular Cavity," J. Fluid Mech., **675**, pp. 369–396.
[47] Jyotsna, R., and Vanka, S. P., 1995, "A Pressure Based Multigrid Procedure for the Navier–Stokes Equations on Unstructured Grids," The 7th Copper Mountain Conference on Multigrid Methods, Copper Mountain, CO, April 2–7, pp. 409.
[48] Glowinski, R., Guidoboni, G., and Pan, T.-W., 2006, "Wall-Driven Incompressible Viscous Flow in a Two-Dimensional Semi-Circular Cavity," J. Comput. Phys., **216**(1), pp. 76–91.
[49] Shinn, A. F., Goodwin, M. A., and Vanka, S. P., 2009, "Immersed Boundary Computations of Shear- and Buoyancy-Driven Flows in Complex Enclosures," Int. J. Heat Mass Transfer, **52**(17), pp. 4082–4089.
[50] Al-Salem, K., Öztop, H. F., Pop, I., and Varol, Y., 2012, "Effects of Moving Lid Direction on MHD Mixed Convection in a Linearly Heated Cavity," Int. J. Heat Mass Transfer, **55**(4), pp. 1103–1112.
[51] Oztop, H. F., Al-Salem, K., and Pop, I., 2011, "MHD Mixed Convection in a Lid-Driven Cavity With Corner Heater," Int. J. Heat Mass Transfer, **54**(15), pp. 3494–3504.
[52] Sivasankaran, S., Malleswaran, A., Lee, J., and Sundar, P., 2011, "Hydro-Magnetic Combined Convection in a Lid-Driven Cavity With Sinusoidal Boundary Conditions on Both Sidewalls," Int. J. Heat Mass Transfer, **54**(1), pp. 512–525.
[53] Yu, P., Qiu, J., Qin, Q., and Tian, Z. F., 2013, "Numerical Investigation of Natural Convection in a Rectangular Cavity Under Different Directions of Uniform Magnetic Field," Int. J. Heat Mass Transfer, **67**, pp. 1131–1144.
[54] Shatrov, V., Mutschke, G., and Gerbeth, G., 2003, "Three-Dimensional Linear Stability Analysis of Lid-Driven Magnetohydrodynamic Cavity Flow," Phys. Fluids, **15**(8), pp. 2141–2151.
[55] Patankar, S. V., and Spalding, D. B., 1972, "A Calculation Procedure for Heat, Mass and Momentum Transfer in Three-Dimensional Parabolic Flows," Int. J. Heat Mass Transfer, **15**(10), pp. 1787–1806.
[56] Leonard, B. P., 1979, "A Stable and Accurate Convective Modelling Procedure Based on Quadratic Upstream Interpolation," Comput. Methods Appl. Mech. Eng., **19**(1), pp. 59–98.
[57] Vanka, S. P., 2013, "2012 Freeman Scholar Lecture: Computational Fluid Dynamics on Graphics Processing Units," ASME J. Fluids Eng., **135**(6), p. 061401.
[58] Shinn, A. F., Vanka, S. P., and Hwu, W. W., 2010, "Direct Numerical Simulation of Turbulent Flow in a Square Duct Using a Graphics Processing Unit (GPU)," AIAA Paper No. 2010-5029.
[59] Vanka, S. P., Shinn, A. F., and Sahu, K. C., 2011, "Computational Fluid Dynamics Using Graphics Processing Units: Challenges and Opportunities," ASME International Mechanical Engineering Congress and Exposition, American Society of Mechanical Engineers, pp. 429–437.
[60] Chaudhary, R., 2011, "Studies of Turbulent Flows in Continuous Casting of Steel With and Without Magnetic Field," Ph.D. thesis, University of Illinois at Urbana-Champaign, IL.
[61] Shinn, A. F., 2011, "Large Eddy Simulations of Turbulent Flows on Graphics Processing Units: Application to Film-Cooling Flows," Ph.D. thesis, University of Illinois at Urbana-Champaign, IL.
[62] Chaudhary, R., Ji, C., Thomas, B. G., and Vanka, S. P., 2011, "Transient Turbulent Flow in a Liquid-Metal Model of Continuous Casting, Including Comparison of Six Different Methods," Metall. Mater. Trans. B, **42**(5), pp. 987–1007.
[63] ANSYS, INC., 2009, ANSYS FLUENT, "12.0 documentation,".

Downloaded From: http://asmedigitalcollection.asme.org/ on 03/26/2015 Terms of Use: http://asme.org/terms